

**¹⁸F-THK5351: A Novel PET Radiotracer for Imaging
Neurofibrillary Pathology in Alzheimer's Disease**

Ryuichi Harada¹, Nobuyuki Okamura^{1,2,3}, Shozo Furumoto⁴, Katsutoshi
Furukawa⁵, Aiko Ishiki⁵, Naoki Tomita⁵, Tetsuro Tago⁴, Kotaro Hiraoka³,
Shoichi Watanuki³, Miho Shidahara^{3,6}, Masayasu Miyake³, Yoichi Ishikawa⁴,
Rin Matsuda³, Akie Inami³, Takeo Yoshikawa², Yoshihito Funaki⁴, Ren Iwata⁴,
Manabu Tashiro³, Kazuhiko Yanai², Hiroyuki Arai⁵, Yukitsuka Kudo^{1,4}

¹Division of Neuro-imaging, Institute of Development, Aging and Cancer,
Tohoku University, Sendai 980-8575, Japan

²Department of Pharmacology, Tohoku University School of Medicine, Sendai
980-8575, Japan

³Division of Cyclotron Nuclear Medicine, Cyclotron and Radioisotope Center,
Tohoku University, Sendai 980-8578, Japan

⁴Division of Radiopharmaceutical Chemistry, Cyclotron and Radioisotope

Center, Tohoku University, Sendai 980-8578, Japan

⁵Department of Geriatrics and Gerontology, Institute of Development, Aging
and Cancer, Tohoku University, Sendai 980-8575, Japan

⁶Division of Medical Physics, Tohoku University School of Medicine, Sendai
980-8575, Japan

Corresponding author:

Nobuyuki Okamura

Department of Pharmacology

Tohoku University School of Medicine

2-1, Seiryō-machi, Aoba-ku, Sendai 980-8575, Japan

Tel: +81-22-717-8058, Fax: +81-22-717-8060

E-mail: nookamura@med.tohoku.ac.jp

First author:

Ryuichi Harada

Division of Neuro-imaging, Institute of Development, Aging and Cancer,

Tohoku University, Sendai 980-8575, Japan

Tel: +81-22-717-7586, Fax: +81-22-717-7586

E-mail: dragon1@med.tohoku.ac.jp

Postdoctoral Fellow

Funding:

This study was supported by research funds from GE Healthcare, the SEI (Sumitomo Electric Industries, Ltd.) Group CSR Foundation, the Industrial Technology Research Grant Program of the NEDO in Japan (09E51025a), Health and Labor Sciences Research Grants from the Ministry of Health, Labor, and Welfare of Japan, Grant-in-Aid for Scientific Research (B) (15H04900), Grant-in-Aid for Scientific Research on Innovative Areas (Brain Protein Aging and Dementia Control) (26117003), Grant-in-Aid for Young Scientists (B) (15K19767), and Grant-in-Aid for JSPS Fellows and “Japan Advanced Molecular Imaging Program (J-AMP)” of the Ministry of Education, Culture,

Sports, Science and Technology (MEXT), Japan.

Word count: 4837

Running title: ^{18}F -THK5351: A Novel Tau PET Tracer

ABSTRACT

Imaging of neurofibrillary pathology in the brain helps in diagnosing dementia, tracking disease progression, and evaluating the therapeutic efficacy of anti-dementia drugs. The radiotracers used in this imaging must be highly sensitive and specific for tau protein fibrils in the human brain. We developed a novel tau PET tracer, ^{18}F -THK5351, through compound optimization of arylquinoline derivatives. **Methods:** The *in vitro* binding properties, pharmacokinetics, and safety of ^{18}F -THK5351 were investigated and a clinical study on Alzheimer disease (AD) patients was performed. **Results:** ^{18}F -THK5351 demonstrated higher binding affinity for hippocampal homogenates from AD brains and faster dissociation from white-matter tissue than did ^{18}F -THK5117. The THK5351 binding amount correlated with the amount of tau deposits in human brain samples. Autoradiography of brain sections revealed that THK5351 bound to neurofibrillary tangles selectively and with a higher signal-to-background ratio than did THK5117. THK5351 exhibited favorable pharmacokinetics and no defluorination in mice. In

first-in-man PET studies in AD patients, ^{18}F -THK5351 demonstrated—compared to ^{18}F -THK5117—faster kinetics, higher contrast, and lower retention in subcortical white matter. **Conclusion:** ^{18}F -THK5351 is a useful PET tracer for early detection of neurofibrillary pathology in AD patients.

Key Words: Alzheimer's disease; tau; PET; radiotracer; ^{18}F -THK5351

INTRODUCTION

Tau accumulation occurs in a stereotyped spatiotemporal manner at the intraneuronal and anatomical distribution levels in the brain and is associated with neuronal loss and cognitive impairment (1-5). Because tau accumulation plays a key role in neurodegeneration and is considered to start before extensive neuronal loss emerges, tau-focused drug-discovery strategies for Alzheimer's disease (AD) are of particular interest (6, 7). In efforts to accelerate drug discovery, there is growing demand for techniques to measure brain tau loads noninvasively. PET imaging of tau is expected to provide spatiotemporal information on the progression of tau pathology in the living brain. Therefore, this technique will facilitate accurate tauopathy diagnosis, precise assessment of disease severity and therapeutic efficacy, and patient enrolment for anti-tau therapeutic trials (8-10).

Several putative tau PET tracers have been developed and tested in humans (11-14), and all of these tracers show elevated uptake in the hippocampus and temporal cortex of AD patients. We screened β -sheet-binding compounds and

identified a series of compounds that preferentially bind to tau deposits in AD brains (15-17). Through compound optimization, several ^{18}F -labeled arylquinoline derivatives were developed as candidate tau PET radiotracers (18). Recent ^{18}F -THK5105 and ^{18}F -THK5117 PET studies demonstrated increased tracer uptake in common sites of tau pathology in AD and its association with clinical severity of dementia (19, 20). However, these tracers—like amyloid PET tracers—showed high nonspecific retention in subcortical white matter. This white-matter binding must be minimized because the signals could obscure visual interpretation of PET images and decrease detection sensitivity for early tau pathology in the presymptomatic stage of AD. For assessing the therapeutic efficacy of potential anti-tau drugs in clinical trials, tau PET tracers must be adequately sensitive to detect even subtle changes in brain tau loads. Moreover, tau PET is expected to detect age-associated neurofibrillary tangles (NFTs) in cognitively normal individuals, recently named primary age-associated tauopathy (21-23). Because such age-related tau pathology is typically milder than disease-related changes in AD, the radiotracers used must

be highly sensitive.

To reduce nonspecific tracer retention in white matter and increase the signal-to-background ratio of PET images, we replaced a benzene ring of ^{18}F -THK5117 with pyridine and developed a novel tau PET tracer, ^{18}F -THK5351. ^{18}F -THK5351 is a single *S*-enantiomer, which should improve the pharmacokinetics of arylquinoline derivatives (Fig. 1). To evaluate the clinical usefulness of ^{18}F -THK5351 as a tau PET tracer, we examined the *in vitro* binding properties, pharmacokinetics, and safety of ^{18}F -THK5351 and performed a clinical study on AD patients.

MATERIAL AND METHODS

Radiosynthesis of Quinoline Derivatives

^{18}F -THK5351 was prepared from its tosylate precursor (*S*)-(2-(2-methylaminopyrid-5-yl)-6-[[2-(tetrahydro-2H-pyran-2-yloxy)-3-tosyloxy]propoxy] quinoline (THK5352) according to the previously described method for synthesizing ^{18}F -THK5105 and ^{18}F -THK5117 (18). ^{18}F -THK5351

was purified using semi-preparative high-performance liquid chromatography (HPLC) (column: Inertsil[®] ODS-4 (GL Sciences, Inc., Tokyo, Japan); mobile phase: 20 mmol/L NaH₂PO₄/acetonitrile (75/25 for THK5351); flow rate: 5.0 mL/min). The radiolabeled product was dissolved in ethanol, DMSO, or saline with polysorbate-80 (<0.1%) for biological evaluation. ¹⁸F-THK5351 was obtained at a radiochemical yield of 46% ± 13% (decay-corrected), radiochemical purity of >95%, and specific activity of 254 ± 47 GBq/μmol. ³H-PiB (specific activity, 2.96 GBq/μmol; radiochemical purity, 99%) was purchased from American Radiolabelled Chemicals (St. Louis, MO). ³H-THK5351 (specific activity, 2.96 TBq/mmol; radiochemical purity, 98.9%) and ³H-THK5117 (specific activity, 2.78 TBq/mmol; radiochemical purity, 98.2%) were custom labeled by Sekisui Medical Inc. (Tokyo, Japan).

***In Vitro* Binding Study**

Experiments were performed as per the regulations of the Ethics Committee of the Tohoku University School of Medicine. Brain samples were obtained

from Tohoku University Brain Bank. The following studies were conducted as described previously: *in vitro* saturation binding assays (18); *in vitro* association and dissociation rate measurement (20, 24); and *in vitro* binding assays, using 1 nmol/L ^3H -labeled ligands (20).

Autoradiography

Experimental procedures followed the regulations of the Ethics Committee of the Tohoku University School of Medicine. Autoradiography in postmortem brain sections was conducted using ^3H -THK5351, ^3H -THK5117, and ^3H -PiB as reported (20). Washing procedures were modified slightly. Briefly, after 30-min incubation at room temperature with 3 nmol/L ^3H -labeled compounds, sections were washed sequentially with PBS containing 1% BSA (5 min) and PBS (5 min, twice). Dried sections were exposed to an imaging plate for 3 days. High-resolution autoradiography of ^3H -labeled sections was performed as before (20).

Small-Animal PET Studies

All animal experiment protocols were approved by the Laboratory Animal Care Committee of Tohoku University. *In vivo* PET studies were performed using male SLC:ICR mice, as described (24).

Biodistribution Studies

Biodistribution was investigated after intravenous injection of ^{18}F -THK5351 or ^{18}F -THK5117 into male ICR mice as previously described (18). Based on the biodistribution data from mice (%ID/g), we estimated the radiation dose and mass dose for humans.

Animal Toxicity Studies

A 14-day toxicity study involving a single-dose THK5351 test-article administration through intravenous injection in ICR mice was performed at Mitsubishi Chemical Medience Corporation (Tokyo, Japan), as described (18).

Radiosynthesis for Clinical PET Study

^{18}F -THK5351, ^{18}F -THK5117, and ^{11}C -PiB were prepared at the Cyclotron and Radioisotope Center, Tohoku University. ^{18}F -THK5351 was radiosynthesized using a semi-automated system developed in-house. No-carrier-added ^{18}F -fluoride ($^{18}\text{F}^-$) produced by the HM-12 cyclotron (30 min/25 μA ; Sumitomo Heavy Industries, Tokyo, Japan) was separated from the irradiated target water by using a Sep-Pak Light Accell Plus QMA cartridge (Waters, Milford, MA). The trapped $^{18}\text{F}^-$ was eluted using a Kryptofix solution (Kryptofix 222 (20 mg), K_2CO_3 (4 mg), MeCN (0.7 mL), H_2O (0.3 mL)) into a reaction vial. The solution was evaporated to dryness through azeotropic distillation with acetonitrile. After drying, THK5352 (3 mg, 5.3 μmol) dissolved in DMSO (0.7 mL) was transferred into the reaction vial and stirred at 110°C for 10 min, and then aq. HCl (2 mol/L, 0.2 mL) was added to the reaction solution and stirred at 110°C for another 3 min. The reaction was then quenched with aq. AcOK (0.8 mol/L, 1 mL) and distilled water (7 mL), after which solid-phase extraction was performed using a Sep-Pak tC18 Plus cartridge

(Waters). The trapped radioactive products were eluted using 60% EtOH, and then the eluate was mixed with H₂O and subjected to semi-preparative HPLC separation under the same conditions as those described above. The HPLC fraction of ¹⁸F-THK5351 was collected in glassware containing H₂O (30 mL) and ascorbic acid (25%, 1.0 mL; NIPRO Pharma, Tokyo, Japan), and ¹⁸F-THK5351 was isolated from the solution through solid-phase extraction performed using a Sep-Pak tC18 Plus cartridge. The ethanol eluate from the cartridge was transferred into a flask containing polysorbate-80 (5% in ethanol, 0.8 mL) and ascorbic acid (25%, 0.2 mL), and then the solution was evaporated to dryness. The radioactive residue was dissolved in saline and sterilized through filtration by using a Millex-GV Syringe Filter Unit (Millipore, Billerica, MA). ¹⁸F-THK5117 was synthesized as described previously (20). ¹¹C-PiB was synthesized by using a loop-method with ¹¹C-methyl triflate, as reported (25). The radiochemical purity of the injectable solutions of ¹⁸F-THK5351, ¹⁸F-THK5117, and ¹¹C-PiB was >95%, and their specific activities were 254 ±

47, 357 ± 270 , and 240 ± 48 GBq/ μ mol, respectively.

Clinical PET Study Participants

Three AD patients and 3 healthy elderly study participants underwent ^{18}F -THK5351 PET scans. Participant demographic data are shown in Supplementary Table 1. Two AD patients underwent additional ^{18}F -THK5117 PET scans within 2-week intervals and additional ^{11}C -PiB PET scans within 3-month intervals. Probable AD was diagnosed based on criteria from the National Institute of Neurological and Communicative Disorders and Stroke and the Alzheimer's Disease Related Disorders Association (NINCDS-ADRDA). This study was approved by the Ethics Committee of the Tohoku University Hospital. The study was fully described to the patients and then written informed consent was obtained from the patients or their guardians.

PET and MRI Image Acquisition

PET imaging was performed using an Eminence STARGATE PET scanner (Shimadzu, Kyoto, Japan). After intravenous injection of ^{18}F -THK5117 (185 MBq), ^{18}F -THK5351 (185 MBq), or ^{11}C -PiB (296 MBq), dynamic PET images were obtained for 90 min (^{18}F -THK5117 and ^{18}F -THK5351) or 70 min (^{11}C -PiB), with the patients' eyes closed. MRI was performed on all participants. T1- and T2-weighted MR images were obtained using a SIGNA 1.5-Tesla machine (General Electric, Milwaukee, WI). In T1-weighted MRI, a 3D volumetric acquisition of a T1-weighted gradient echo sequence produced a gapless series of thin axial sections by using a vascular TOF SPGR sequence (echo time/repetition time, 2.4/50 ms; flip angle, 45° ; acquisition matrix, 256×256 ; 1 excitation; field of view, 22 cm; slice thickness, 2.0 mm).

Image Analysis

Standardized uptake value (SUV) images of ^{18}F -THK5117, ^{18}F -THK5351, and ^{11}C -PiB were obtained by normalizing tissue radioactivity concentration by injected dose and bodyweight. MRI T1 images were coregistered to the early

PET images (0–10 min post-injection) for each participant by using statistical parametric-mapping software (SPM8; Wellcome Department of Imaging Neuroscience, UCL, London, UK). PET images were processed using a semi-automatic region-of-interest method, as described (19). The regional SUV to cerebellar cortex SUV ratio (SUVR) was used as an index of tracer retention. Coregistered MRI and PET images were spatially normalized to an MRI T1 template in Talairach space by using SPM8. After spatial normalization, regional SUVs were sampled using PMOD software. Regions of interest were placed on individual axial images in the cerebellar hemisphere, dorsolateral prefrontal cortex (Brodmann's area (BA) 9), ventrolateral prefrontal cortex (BA 10, 44, 45, and 46], orbitofrontal cortex (BA 11 and 12), superior temporal cortex (BA 22), inferior temporal cortex (BA 20 and 37), parietal cortex (BA 39 and 40), occipital cortex (BA 17, 18, and 19), anterior cingulate cortex, posterior cingulate cortex, parahippocampal gyrus, and subcortical white matter.

Statistical Analysis

Pearson correlation coefficients were calculated to assess the relationship between ^3H -labeled tracer binding and the amounts of insoluble protein. Spearman correlation coefficients were calculated to assess the relationship between tracer retentions in AD patients.

RESULTS

In Vitro Tracer Binding to Human Brain Tissues

In vitro saturation binding assays were conducted to measure the binding affinity of ^{18}F -THK5351 for postmortem tissues from AD patients. Scatchard analysis indicated one-site binding of ^{18}F -THK5351 for postmortem hippocampal homogenates from an AD patient (Suppl. Fig. 1A). ^{18}F -THK5351 bound to AD hippocampal homogenates with high affinity ($K_d = 2.9$ nmol/L; $B_{\max} = 368.3$ pmol/g tissue). We measured the *in vitro* binding of ^3H -labeled THK5351 and THK5117 to postmortem tissues from 8 AD patients in order to compare the amount of specific binding of these tracers; the tracers were used

at 1 nmol/L, the concentration typically achieved during PET scans. The specific binding of THK5351 and THK5117 was highly correlated ($r = 0.98$, $P < 0.0001$) (Suppl. Fig. 1B). The specific binding of THK5351 was also correlated with the level of insoluble tau ($r = 0.71$, $P < 0.05$), but not insoluble amyloid- β ($r = -0.20$, $P = 0.63$) or PiB ($r = -0.10$, $P = 0.82$), as observed for THK5117 (20). Furthermore, *in vitro* dissociation assays performed using brain white-matter homogenates revealed that THK5351 dissociated from white matter more rapidly than THK5117 did (Fig. 2A).

In Vitro Autoradiography in Human Brain Sections

To further evaluate binding selectivity and signal-to-background ratio, *in vitro* autoradiography was performed using ^3H -THK5351 and ^3H -THK5117 exhibiting similar specific activity; here, postmortem brain sections from a control participant and AD patients were used. Both ^3H -THK5351 and ^3H -THK5117 bound to the gray matter of AD brain sections in a laminar fashion, which corresponded to tau immunohistochemistry. However, in

contrast to the substantial white-matter binding of ^3H -THK5117, only weak ^3H -THK5351 signals were detected in white matter (Fig. 2B). ^3H -THK5351 showed higher cortical-to-white matter binding ratio than ^3H -THK5117 did (Fig. 2C). ^3H -THK5351 also showed little binding to control brain sections. Microautoradiography of AD brain sections provided additional evidence supporting the ability of ^3H -THK5351 to selectively label NFTs. The ^3H -THK5351 labeling patterns resembled the Gallyas–Braak staining in adjacent sections (Fig. 3). However, ^3H -THK5351 did not label amyloid plaques that were labeled with ^3H -PiB in an adjacent section. Furthermore, autoradiography of hemibrain sections from an AD patient demonstrated preferential ^3H -THK5351 binding in the gray matter of the hippocampus, parahippocampal gyrus, fusiform gyrus, inferior and middle temporal gyri, insula, and cingulate gyrus, regions that contain a high density of tau deposits in AD (Suppl. Fig. 2). These tracer-binding patterns differed completely from the broad neocortical binding of ^{11}C -PiB.

Pharmacokinetics in Mice

Brain pharmacokinetics of ^{18}F -THK5351 in normal mice were investigated using a small-animal PET scanner. Although the peak brain uptake of ^{18}F -THK5351 was slightly lower than that of ^{18}F -THK5117, ^{18}F -THK5351 entered the brain immediately after intravenous injection and showed faster washout from the brain than ^{18}F -THK5117 did (Fig. 4; Suppl. Table 2). No marked radiotracer retention in bone was observed after ^{18}F -THK5351 was injected into mice.

Animal Acute-Toxicity Studies

At 0.1 and 1 mg/kg dosages under our study conditions, no animals died and no treatment-related changes in any animal were noted in clinical observations, bodyweight measurement, and pathological examination.

Dose Estimates for Humans

^{18}F -THK5351 radiation exposure was estimated using the biodistribution data from mice (Suppl. Table 2). The resultant whole-body effective dose equivalents were 14.4 $\mu\text{Sv}/\text{MBq}$ (male) and 18.4 $\mu\text{Sv}/\text{MBq}$ (female) (Suppl. Table 3). The organ doses for ^{18}F -THK5351 were comparable to those associated with other common radiotracers.

Clinical PET Study

The SUV time-activity curves from ^{18}F -THK5351 and ^{18}F -THK5117 PET in 2 patients are shown in Fig. 5. The pharmacokinetic data agreed with the small-animal PET study in normal mice. The peak uptake of ^{18}F -THK5351 was again slightly lower than that of ^{18}F -THK5117, but ^{18}F -THK5351 was cleared more rapidly than ^{18}F -THK5117 from the cerebellar cortex. In the AD patients, ^{18}F -THK5351 binding in the inferior temporal cortex exceeded white-matter binding at all the time points after injection.

PET images are shown in Fig. 6. ^{18}F -THK5351 retention in the temporal lobe clearly distinguished AD patients from healthy elderly participants,

although mild ^{18}F -THK5351 retention was observed in the medial temporal cortex of elderly healthy control subjects (Fig. 6A). ^{18}F -THK5351 showed higher contrast and lower subcortical white-matter retention than ^{18}F -THK5117 did (Fig. 6B). ^{18}F -THK5351 and ^{18}F -THK5117 retention was particularly prominent in the mesial temporal lobe and the lateral temporal cortex, which differed considerably from ^{11}C -PiB retention in the same AD patient (Table 1): ^{11}C -PiB exhibited extremely high retention throughout broad neocortical areas except for the mesial temporal lobe. The regional SUVR values of ^{18}F -THK5351 were higher than those of ^{18}F -THK5117 (Table 1), and the regional SUVR of ^{18}F -THK5351 in 2 AD patients was significantly correlated with that of ^{18}F -THK5117 (Spearman's $r = 0.839$, $P < 0.001$), but not that of ^{11}C -PiB (Fig. 7).

DISCUSSION

^{18}F -THK5351 is a single *S*-enantiomer and pyridine derivative of ^{18}F -THK5117, and ^{18}F -THK5351 is less lipophilic than ^{18}F -THK5117 (Log $P =$

1.5 vs 2.32). As observed with amyloid PET tracers, pyridine derivatives tend to show reduced lipophilicity, which correlates with the amount of nonspecific binding (26). Replacement of the 2-aryl group from the benzene to the pyridine ring might contribute to diminished nonspecific binding to subcortical white matter, as observed in the relationship between ^{11}C -PiB and ^{11}C -AZD2184 (27-29). Moreover, ^{18}F -THK5351 is optically pure, whereas ^{18}F -THK5105 and ^{18}F -THK5117 are racemic mixtures. Enantiomers frequently show differences in biological properties such as metabolism or binding affinity for targets (30). Our preclinical studies demonstrated that the pharmacokinetic profiles of the *S*-enantiomers of arylquinoline derivatives were more favorable than those of the *R*-enantiomers (20, 24). Therefore, optical purification should additionally contribute toward improving THK5351 pharmacokinetics. Our preclinical data revealed that ^{18}F -THK5351 shows high and selective binding ability for tau aggregates, low binding affinity for white matter, and rapid pharmacokinetics, which collectively resulted in the signal-to-background ratio of THK5351 being higher than that of both THK5105 and THK5117. Furthermore,

autoradiography performed on human brain sections also confirmed that THK5351 does not bind to amyloid, α -synuclein, and TDP43 deposits (data not shown), which suggests that THK5351 binds to tau protein fibrils with high selectivity.

As observed in our previous ^{18}F -THK5105 and ^{18}F -THK5117 PET studies (19, 20), ^{18}F -THK5351 retention was prominent in the temporal lobe of AD patients. This regional distribution of ^{18}F -THK5351 in AD patients agreed with the postmortem observation that the temporal lobe was more susceptible to tau deposition than other cortical areas (31, 32). Although the cortical distributions of ^{18}F -THK5351 and ^{18}F -THK5117 in the same patients were almost identical, ^{18}F -THK5351 displayed comparatively higher contrast and lower subcortical white-matter retention; this is strikingly similar to our preclinical findings (Figs. 2–4). When compared with reported tau radiotracers such as ^{11}C -PBB3 and ^{18}F -T807, a drawback of ^{18}F -THK5117 is high white-matter retention, which is frequently observed with ^{18}F -labeled amyloid radiotracers (33). The cortical-to-white matter ratio of ^{18}F -THK5351 in AD patients was substantially

higher than that of ^{18}F -THK5117, which allows comparatively easier and more accurate visual interpretation of PET images. No remarkable retention of ^{18}F -THK5351 was observed in the choroid plexus or venous sinus. This is one of the advantages over the other tau tracers, because off-target retention in these areas might cause a spill-in of the tracer signals into the brain. However, as observed with other radiotracers, off-target binding of ^{18}F -THK5351 was detected in the basal ganglia; the binding target of THK5351 in this region should be clarified in future studies. Moreover, ^{18}F -THK5351 must be directly compared with other tau radiotracers to characterize the binding property of each radiotracer and to determine how their differences affect the accuracy of visual interpretation and the sensitivity for detecting subtle changes in brain tau loads over time, as done in the case of amyloid radiotracers (34-36). Furthermore, imaging-autopsy studies are required to validate the described binding selectivity in the future.

CONCLUSION

¹⁸F-THK5351 selectively bound to pathological tau deposits in postmortem AD brain tissues, but showed weak white-matter binding. Fast pharmacokinetics, high contrast, and low white-matter retention of ¹⁸F-THK5351 allow sensitive detection of tau pathology in humans, which could facilitate early detection and longitudinal assessment of neurofibrillary pathology.

DISCLOSURE

This study was supported by research funds from GE Healthcare, the SEI (Sumitomo Electric Industries, Ltd.) Group CSR Foundation, the Industrial Technology Research Grant Program of the NEDO in Japan (09E51025a), Health and Labor Sciences Research Grants from the Ministry of Health, Labor, and Welfare of Japan, Grant-in-Aid for Scientific Research (B) (15H04900), Grant-in-Aid for Scientific Research on Innovative Areas (Brain Protein Aging and Dementia Control) (26117003), Grant-in-Aid for Young Scientists (B)

(15K19767), and Grant-in-Aid for JSPS Fellows and “Japan Advanced Molecular Imaging Program (J-AMP)” of the Ministry of Education, Culture, Sports, Science and Technology (MEXT), Japan.

REFERENCES

1. Braak H, Braak E. Neuropathological staging of Alzheimer-related changes. *Acta Neuropathol.* 1991;82:239-259.
2. Braak E, Braak H, Mandelkow EM. A sequence of cytoskeleton changes related to the formation of neurofibrillary tangles and neuropil threads. *Acta Neuropathol.* 1994;87:554-567.
3. Braak H, Alafuzoff I, Arzberger T, Kretschmar H, Del Tredici K. Staging of Alzheimer disease-associated neurofibrillary pathology using paraffin sections and immunocytochemistry. *Acta Neuropathol.* 2006;112:389-404.
4. Delacourte A, David JP, Sergeant N, et al. The biochemical pathway of neurofibrillary degeneration in aging and Alzheimer's disease. *Neurology.* 1999;52:1158-1165.
5. Guillozet AL, Weintraub S, Mash DC, Mesulam MM. Neurofibrillary tangles, amyloid, and memory in aging and mild cognitive impairment. *Arch Neurol.* 2003;60:729-736.
6. Brunden KR, Trojanowski JQ, Lee VM. Advances in tau-focused drug discovery for Alzheimer's disease and related tauopathies. *Nat Rev Drug Discov.* 2009;8:783-793.
7. Giacobini E, Gold G. Alzheimer disease therapy-moving from amyloid- β to tau. *Nat Rev Neurol.* 2013;9:677-686.
8. Okamura N, Harada R, Furumoto S, Arai H, Yanai K, Kudo Y. Tau PET imaging in Alzheimer's disease. *Curr Neurol Neurosci Rep.* 2014;14:500.
9. Villemagne VL, Fodero-Tavoletti MT, Masters CL, Rowe CC. Tau imaging: early progress and future directions. *Lancet Neurol.* 2015;14:114-124.
10. Ariza M, Kolb HC, Moechars D, Rombouts F, Andres JI. Tau positron emission tomography (PET) imaging: past, present, and future. *J Med Chem.* 2015;58:4365-4382.
11. Chien DT, Bahri S, Szardenings AK, et al. Early clinical PET imaging results with the novel PHF-tau radioligand [F-18]-T807. *J Alzheimers Dis.* 2013;34:457-468.

12. Chien DT, Szardenings AK, Bahri S, et al. Early clinical PET imaging results with the novel PHF-tau radioligand [F18]-T808. *J Alzheimers Dis.* 2014;38:171-184.

13. Maruyama M, Shimada H, Suhara T, et al. Imaging of tau pathology in a tauopathy mouse model and in Alzheimer patients compared to normal controls. *Neuron.* 2013;79:1094-1108.

14. Villemagne VL, Furumoto S, Fodero-Tavoletti MT, et al. *In vivo* evaluation of a novel tau imaging tracer for Alzheimer's disease. *Eur J Nucl Med Mol Imaging.* 2014;41:816-826.

15. Okamura N, Suemoto T, Furumoto S, et al. Quinoline and benzimidazole derivatives: candidate probes for *in vivo* imaging of tau pathology in Alzheimer's disease. *J Neurosci.* 2005;25:10857-10862.

16. Fodero-Tavoletti MT, Okamura N, Furumoto S, et al. ¹⁸F-THK523: a novel *in vivo* tau imaging ligand for Alzheimer's disease. *Brain.* 2011;134:1089-1100.

17. Harada R, Okamura N, Furumoto S, et al. Comparison of the binding characteristics of [¹⁸F]THK-523 and other amyloid imaging tracers to Alzheimer's disease pathology. *Eur J Nucl Med Mol Imaging.* 2013;40:125-132.

18. Okamura N, Furumoto S, Harada R, et al. Novel ¹⁸F-labeled arylquinoline derivatives for noninvasive imaging of tau pathology in Alzheimer disease. *J Nucl Med.* 2013;54:1420-1427.

19. Okamura N, Furumoto S, Fodero-Tavoletti MT, et al. Non-invasive assessment of Alzheimer's disease neurofibrillary pathology using ¹⁸F-THK5105 PET. *Brain.* 2014;137:1762-1771.

20. Harada R, Okamura N, Furumoto S, et al. [¹⁸F]THK-5117 PET for assessing neurofibrillary pathology in Alzheimer's disease. *Eur J Nucl Med Mol Imaging.* 2015;42:1052-1061.

21. Kuzuhara S, Ihara Y, Toyokura Y, Shimada H. [A semiquantitative study on Alzheimer neurofibrillary tangles demonstrated immunohistochemically with anti-tau antibodies, in the brains of non-demented and demented old people]. *No To Shinkei.* 1989;41:465-470.

22. Morris JC, Price JL. Pathologic correlates of nondemented aging, mild cognitive impairment, and early-stage Alzheimer's disease. *J Mol Neurosci.* 2001;17:101-118.

23. Crary JF, Trojanowski JQ, Schneider JA, et al. Primary age-related tauopathy (PART): a common pathology associated with human aging. *Acta Neuropathol.* 2014;128:755-766.

24. Tago T, Furumoto S, Okamura N, et al. Preclinical evaluation of [¹⁸F]THK-5105 enantiomers: effects of chirality on its effectiveness as a tau imaging radiotracer. *Mol Imaging Biol.* 2015. In press.

25. Verdurand M, Bort G, Tadino V, Bonnefoi F, Le Bars D, Zimmer L. Automated radiosynthesis of the Pittsburgh compound-B using a commercial synthesizer. *Nucl Med Commun.* 2008;29:920-926.

26. Forsberg A, Jureus A, Cselenyi Z, et al. Low background and high contrast PET imaging of amyloid- β with [¹¹C]AZD2995 and [¹¹C]AZD2184 in Alzheimer's disease patients. *Eur J Nucl Med Mol Imaging.* 2013;40:580-593.

27. Klunk WE, Engler H, Nordberg A, et al. Imaging brain amyloid in Alzheimer's disease with Pittsburgh Compound-B. *Ann Neurol.* 2004;55:306-319.

28. Nyberg S, Jonhagen ME, Cselenyi Z, et al. Detection of amyloid in Alzheimer's disease with positron emission tomography using [¹¹C]AZD2184. *Eur J Nucl Med Mol Imaging.* 2009;36:1859-1863.

29. Johnson AE, Jeppsson F, Sandell J, et al. AZD2184: a radioligand for sensitive detection of β -amyloid deposits. *J Neurochem.* 2009;108:1177-1186.

30. Simonyi M, Fitos I, Visy J. Chirality of bioactive agents in protein-binding storage and transport processes. *Trends Pharmacol Sci.* 1986;7:112-116.

31. Wilcock GK, Esiri MM. Plaques, tangles and dementia. A quantitative study. *J Neurol Sci.* 1982;56:343-356.

32. Arnold SE, Hyman BT, Flory J, Damasio AR, Van Hoesen GW. The topographical and neuroanatomical distribution of neurofibrillary tangles and neuritic plaques in the cerebral cortex of patients with Alzheimer's disease.

Cereb Cortex. 1991;1:103-116.

33. Rowe CC, Villemagne VL. Brain amyloid imaging. *J Nucl Med.* 2011;52:1733-1740.

34. Villemagne VL, Mulligan RS, Pejoska S, et al. Comparison of ¹¹C-PiB and ¹⁸F-florbetaben for A β imaging in ageing and Alzheimer's disease. *Eur J Nucl Med Mol Imaging.* 2012;39:983-989.

35. Wolk DA, Zhang Z, Boudhar S, Clark CM, Pontecorvo MJ, Arnold SE. Amyloid imaging in Alzheimer's disease: comparison of florbetapir and Pittsburgh compound-B positron emission tomography. *J Neurol Neurosurg Psychiatry.* 2012;83:923-926.

36. Rowe CC, Pejoska S, Mulligan RS, et al. Head-to-head comparison of ¹¹C-PiB and ¹⁸F-AZD4694 (NAV4694) for β -amyloid imaging in aging and dementia. *J Nucl Med.* 2013;54:880-886.

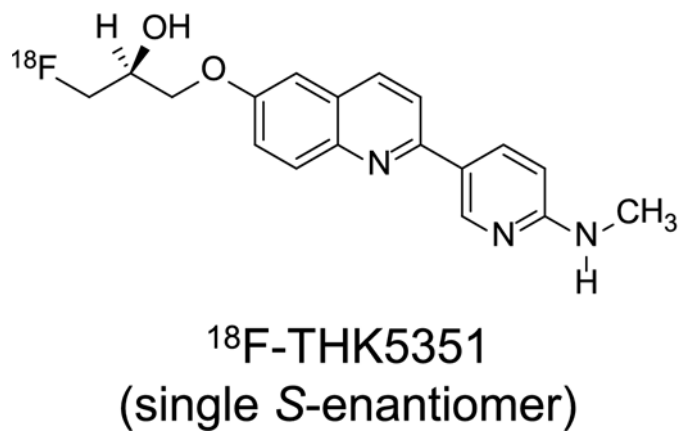
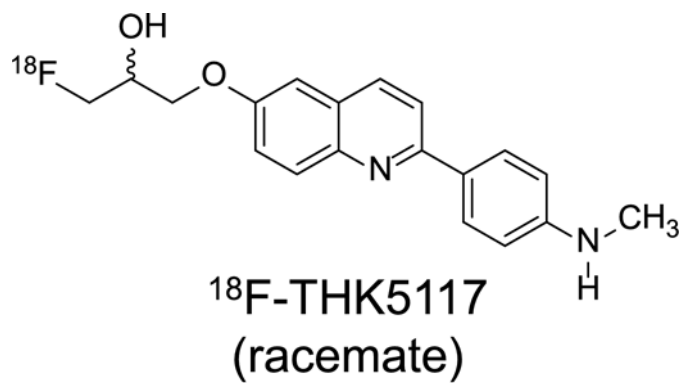


FIGURE 1. ^{18}F -THK5351 and ^{18}F -THK5117 chemical structures.

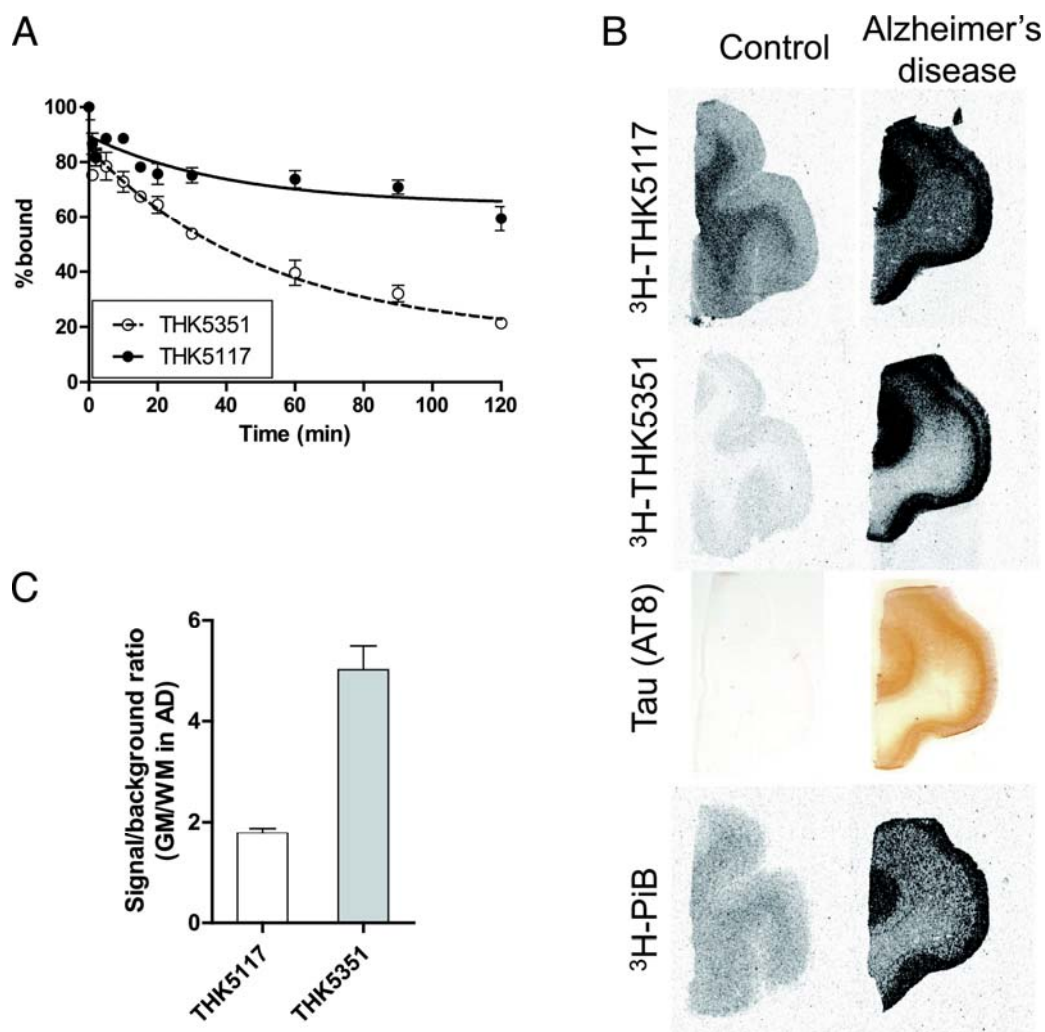


FIGURE 2. (A) *In vitro* dissociation of ^{18}F -THK5351 and ^{18}F -THK5117 from white-matter homogenates from a normal brain. (B) Autoradiography of ^3H -THK5117, ^3H -THK5351, and ^3H -PiB and tau (AT8) immunostaining in frontal brain sections from a control participant and an AD patient. (C) Signal-to-background ratios of ^3H -labeled THK tracers in sections from an AD

patient (Braak stage V). Signal-to-background ratio was calculated as the intensity of tracer binding in gray matter divided by that in subcortical white matter.

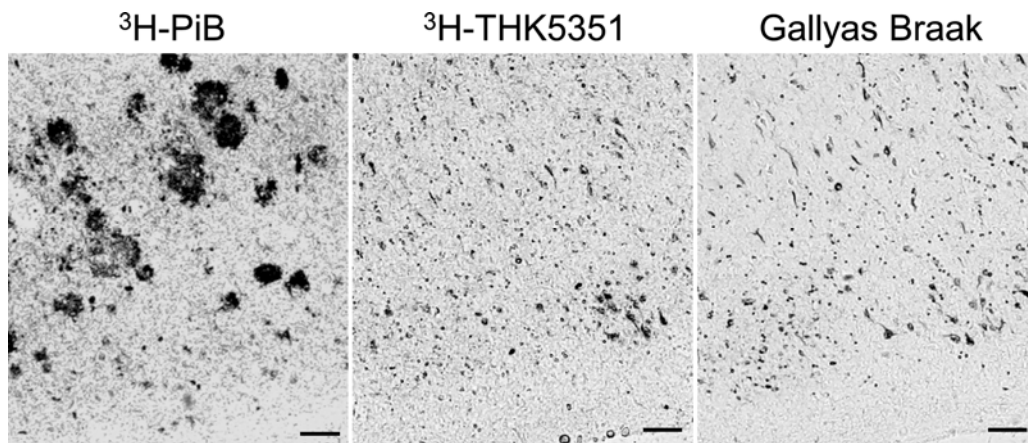


FIGURE 3. High-resolution autoradiography of $^3\text{H-PiB}$ and $^3\text{H-THK5351}$ and Gallyas Braak silver staining in the entorhinal cortex of an AD patient.

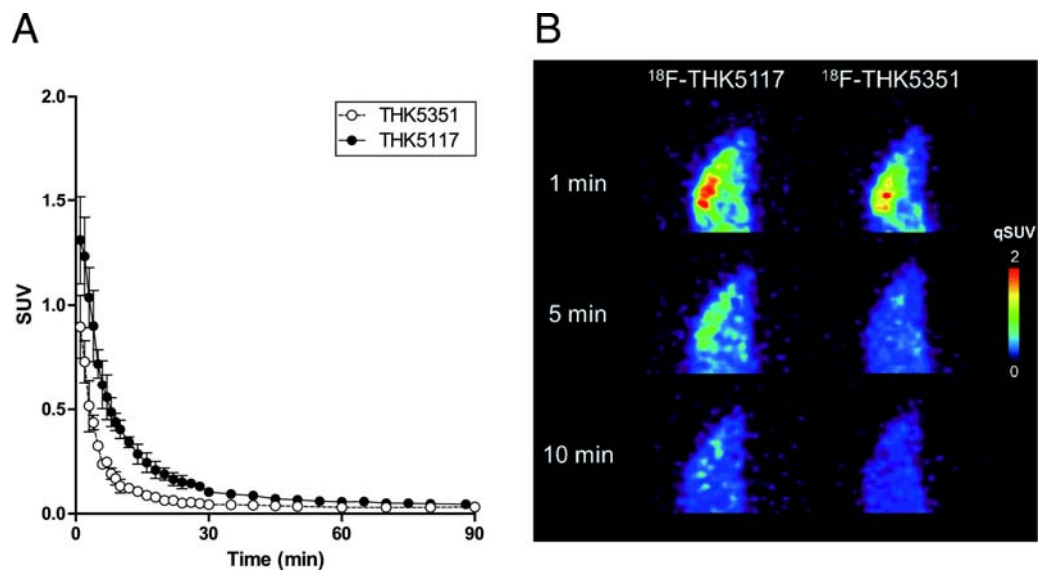


FIGURE 4. (A) Brain time-activity curves after intravenous administration of ^{18}F -THK5351 and ^{18}F -THK5117 in normal mice ($n = 4$). (B) Representative PET images of ^{18}F -THK5117 and ^{18}F -THK5351 at 1, 5, and 10 min post-injection in normal mice.

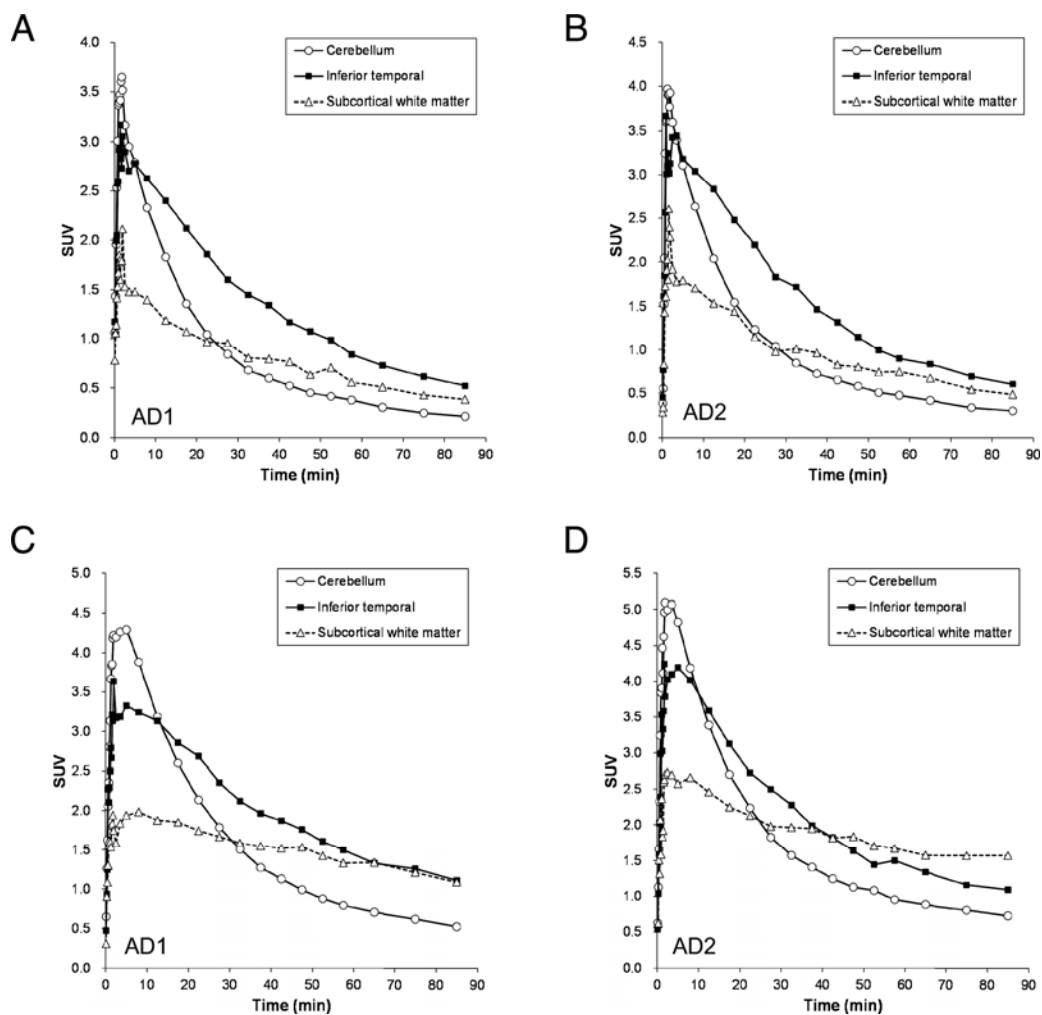


FIGURE 5. $^{18}\text{F-THK5351}$ (A and B) and $^{18}\text{F-THK5117}$ (C and D) SUV time-activity curves in the cerebellum (empty circle), inferior temporal cortex (filled square), and subcortical white matter (empty triangle) of 2 AD patients (AD1: 88-year-old man, MMSE score 25; AD2: 58-year-old man, MMSE score 19).

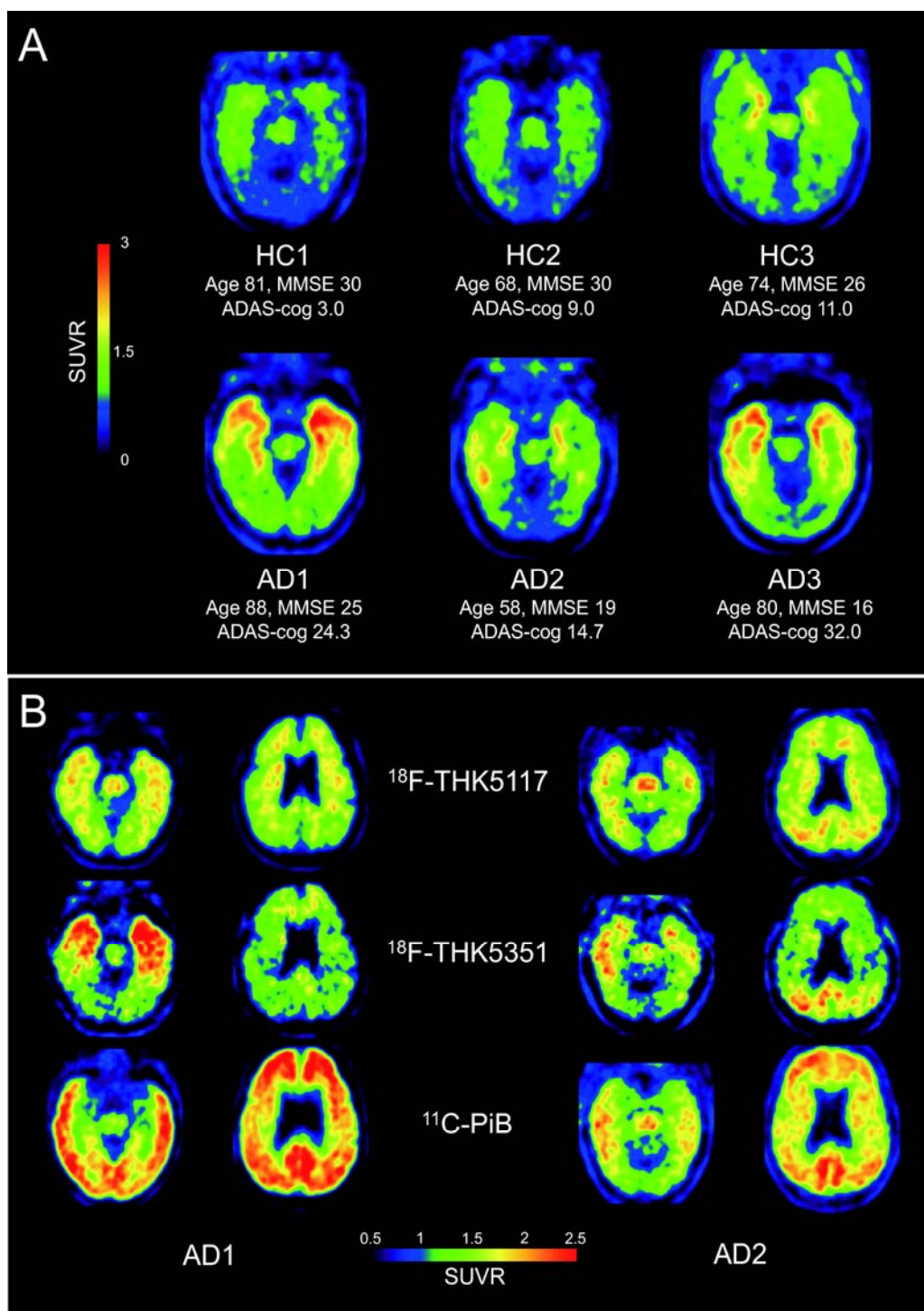


FIGURE 6. (A) SUVR images of ^{18}F -THK5351 PET from 40–60 min post-injection in 3 healthy control (HC) participants and 3 AD patients. (B) SUVR images of ^{18}F -THK5117 and ^{18}F -THK5351 PET from 50–60 min post-injection and ^{11}C -PiB PET from 40–70 min post-injection in 2 AD patients (AD1: 88-year-old man, MMSE score 25; AD2: 58-year-old man, MMSE score 19).

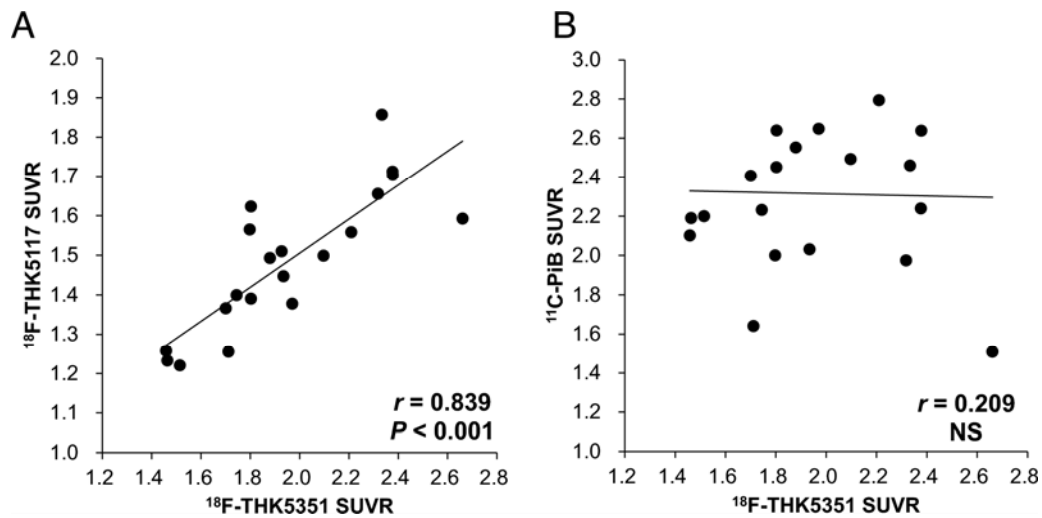


FIGURE 7. Correlation between the regional SUVR of ^{18}F -THK5351 and ^{18}F -THK5117 (Spearman's $r = 0.839$, $P < 0.001$), but not ^{18}F -THK5351 and ^{11}C -PiB ($r = 0.209$, not significant), in 2 AD patients.

TABLE 1 Regional SUVR values (50–60 min post-injection) of ^{18}F -THK5117, ^{18}F -THK5351, and ^{11}C -PiB in 3 HC and 3 AD patients

Region	HC1	HC2	HC3	AD1		AD2			AD3	
	THK5351	THK5351	THK5351	THK5351	THK5117	PiB	THK5351	THK5117	PiB	THK5351
Dorsolateral prefrontal	1.16	1.15	1.36	1.46	1.23	2.19	1.46	1.26	2.10	1.81
Ventrolateral prefrontal	1.28	1.19	1.35	1.93	1.51	3.11	1.70	1.37	2.41	2.03
Orbitofrontal	1.08	1.16	1.45	1.80	1.39	2.64	1.51	1.22	2.20	1.59
Superior temporal	1.36	1.55	1.51	1.88	1.49	2.55	1.80	1.56	2.00	1.67
Inferior temporal	1.44	1.51	1.67	2.33	1.86	2.46	1.93	1.45	2.03	2.36
Parietal	1.43	1.40	1.39	2.21	1.56	2.79	2.38	1.71	2.24	2.22
Occipital	1.26	1.27	1.37	1.80	1.62	2.45	1.71	1.26	1.64	1.68
Posterior cingulate	1.32	1.41	1.63	1.97	1.38	2.65	2.38	1.70	2.64	2.48
Anterior cingulate	1.41	1.54	1.53	2.10	1.50	2.49	1.74	1.40	2.23	1.76
Parahippocampal gyrus	1.85	1.92	2.03	2.66	1.59	1.51	2.32	1.66	1.97	1.82
Hippocampus	1.96	2.03	2.44	3.17	1.71	1.17	2.49	1.64	1.33	3.28
Subcortical white matter	1.42	1.36	1.60	1.61	1.65	1.81	1.52	1.66	2.16	1.38